Comparative efficiency of polycyclic aromatic hydrocarbon removal by novel graphene oxide composites prepared from conventional and green synthesis

Ruth Nóbrega Queiroz [a], Tauany de Figueiredo Neves [b], Meuris Gurgel Carlos da Silva [a], Valmor Roberto Mastelaro [c], Melissa Gurgel Adeodato Vieira [a], Patrícia Prediger [b,*]

[a] *Process and Product Development Department, School of Chemical Engineering, University of Campinas – UNICAMP, Albert Einstein Avenue, 500, 13083-852, Campinas, São Paulo, Brazil*
[b] *School of Technology, University of Campinas – UNICAMP, 13484-332, Limeira, São Paulo, Brazil*
[c] *São Carlos Institute of Physics, University of São Paulo, Av. Trabalhador São Carlense, 400, São Carlos, SP, 13566-590, Brazil*

A B S T R A C T

New materials have been developed based on the pillars of green chemistry; however, few studies compare the potential of these materials with that of conventional materials. In this study, two composites based on graphene oxide and magnetic chitosan were synthesized, one by the green route (G-mCS/GO) and the other by the conventional route (C-mCS/GO), using proanthocyanidin (PAS) and glutaraldehyde as crosslinking agents, respectively. Then, they were applied as adsorbents in the removal of polycyclic aromatic hydrocarbons (PAHs) from synthetic wastewater to compare their performance. Through XRD analysis, the crystallographic properties were obtained, FT-IR analyses indicated the presence of functional groups associated with graphene oxide, chitosan and Fe_3O_4 particles, and the magnetization curves indicated greater saturation magnetization for G-mCS/GO. Adsorption assays were performed at 298 K for 30 min at pH 6.5, an adsorbent dosage of 0.1 mg mL^{-1} and an initial PAH concentration of 0.01 mmol. L^{-1} showed a greater adsorptive capacity of G-mCS/GO for naphthalene (0.093 mmol g^{-1}) and anthracene (0.089 mmol g^{-1}), with removal efficiencies of 93.55% and 89.25%, respectively. On the other hand, C-mCS/GO showed a better removal efficiency for fluoranthene (0.076 mmol g^{-1}), 76.07%. The results obtained through the molecular simulation indicated that naphthalene molecules have greater stability than anthracene and fluoranthene, which contributes to increasing the hydrophobic and π-π interactions between the PAH molecules and the adsorbent surface, thus inducing an increase in the adsorptive capacity. The results of this study indicate that G-mCS/GO is a potential and sustainable adsorbent for PAH removal from wastewater.

1. Introduction

Polycyclic aromatic hydrocarbons (PAHs) are organic compounds formed mainly through anthropogenic activities, which involve pyrolyzis and petrogenic processes (exploration and production of oil and gas). Despite being found in relatively low concentrations, these pollutants are highly toxic and carcinogenic contaminants that can cause damage to human health and the environment when present in industrial effluents, especially those from the petroleum industry. 16 PAHs were listed by the United States Environmental Protection Agency (US EPA) as emerging pollutants, including naphthalene, anthracene and fluoranthene (Queiroz et al., 2022).

Different technologies, such as bioremediation (Song et al., 2021), membrane separation (Li et al., 2019), advanced oxidation processes (AOPs) (Haneef et al., 2020), coagulation-flocculation (Wang et al., 2020) and adsorptive processes (Li et al., 2020), have been studied to efficiently remove PAHs from industrial effluents. Among these technologies, adsorption processes are being increasingly studied due to their high selectivity, low production cost, easy adsorbent recovery and high efficiency (Brião et al., 2018). Graphene-based materials, especially graphene oxide (GO), have been applied as adsorbents for the removal of contaminants due to their characteristics, such as high surface area,

chemical stability, presence of oxygenated functional groups, mechanical resistance and low production cost (Song et al., 2021). These characteristics are responsible for the excellent adsorptive properties for the removal of organic compounds from wastewater, which have attracted the attention of researchers to its application in PAH adsorption: fluoranthene (Hsu et al., 2019); naphthalene and anthracene (Adeola and Forbes, 2022); naphthalene (Maswanganyi et al., 2021); phenanthrene (Huang et al., 2019); and anthracene (Song et al., 2021).

Chitosan is a biodegradable polymer obtained through the deacetylation of chitin, which allows its application in different processes. It can be applied as a flocculant, coagulant and adsorbent for the removal of contaminants such as toxic metals, dyes, pesticides, antibiotics and organic contaminants (Pal et al., 2020). Therefore, the combination of GO with chitosan can contribute to modifying the characteristics of GO, considerably improving its performance in removing organic pollutants and thus increasing the efficiency of the adsorption process (Neves et al., 2020).

The application of natural agents in the synthesis of adsorbent materials has been highlighted in recent years as an alternative methodology to minimize the use of toxic chemical reagents (Queiroz et al., 2022). Plant extracts, microorganisms and agricultural waste have a variety of active compounds and metabolites that can act as stabilizing, crosslinking or capping agents in the synthesis processes, thus enabling the development of new composites with high efficiency, eco-friendliness and low cost (Shi et al., 2020; Zhang et al., 2021).

Therefore, in this study, the synthesis of two composites based on graphene oxide (GO) and magnetic chitosan (mCS) was performed, one by the green route using the extract of water hyacinth (*Eichhornia crassipes*) and proanthocyanidin (PAS) as a stabilizing agent and crosslinking, respectively, and another by the conventional route using glutaraldehyde as a crosslinking agent. The adsorbents were applied for the removal of PAHs from synthetic wastewater to compare the adsorptive performance of both materials. Naphthalene, anthracene and fluoranthene were selected as PAHs in the study, and their physicochemical and structural properties were evaluated through a molecular simulation. The adsorptive affinity assay results were evaluated along with the molecular simulation results to determine the possible mechanisms that govern the adsorptive processes.

2. Materials and methods

2.1. Materials and reagents

Mineral graphite micrograf 99507 UJ - (Nacional Grafite Ltda., Limeira, SP, Brasil); Concentrated sulfuric acid (H_2SO_4) - (ACS); Potassium persulfate (K_2SO_4) - (ACS); Phosphorus pentoxide (P_2O_5) (high purity, 99%) - (Sigma Aldrich); Sodium nitrate ($NaNO_3$) - (ACS); Potassium permanganate ($KMnO_4$) (high purity, 99%) - (CRQ Eireli Chemical Products); Hydrogen peroxide (H_2O_2) (Grade II, 30% w/w) - (Sigma Aldrich); Hydrochloric acid (HCl) (37%) - (ACS); Iron (II) chloride ($FeCl_2.4H_2O$) - (Dynamics); Iron (III) chloride ($FeCl_3.6H_2O$) - (Sigma Aldrich); Ammonium hydroxide (NH_4OH) (28%) - (CRQ Eireli Chemical Products); Chitosan (CS) - (low molecular weight, 75–85% deacetylated, Sigma Aldrich, Code: 448869); Liquid Vaseline (mineral oil) - (Dynamics); Oleic acid - (Synth); Acetic acid (CH_3COOH) (60%) - (Synth); Glutaraldehyde (Grade II, 25% w/w) - (Sigma Aldrich); Pure petroleum ether (30–60 °C) - (Sigma Aldrich); Sodium hydroxide (NaOH) (high purity, 99.99%) - (Synth); Dry N,N-dimethylformamide (DMF) (anhydrous, 99.8%) - (Sigma Aldrich); N,N-dicyclohexylcarbodiimide (DCC) (high purity, 99%) - (Sigma Aldrich); 4-dimethylaminopyridine (DMAP) (high purity, 99%) - (Sigma Aldrich); Methanol (CH_3OH) (P.A.) - (ACS); ethanol (C_2H_5OH) (technical grade, 99%) - (Sigma Aldrich); acetone (C_3H_6O) (P.A.) - (ACS); water hyacinth extract (*Eichhornia crassipes*) - (UNICAMP, Limeira, SP, Brazil); proanthocyanidin (PAS) - (Galena); naphthalene (NAP) (purity, 99%) - (Sigma Aldrich); anthracene (ANT) (purity, 99%) - (Sigma Aldrich);

fluoranthene (FLT) (purity, 99%) - (Sigma Aldrich); methanol (CH_3OH) (HPLC Grade) – (ACS); acetonitrile (C_2H_3N) (HPLC Grade) – (ACS); ultrapure water (OS20LXE, Gehaka).

2.2. Preparation of conventional and green mCS/GO

A schematic diagram of the steps involved in the conventional and green mCS/GO synthesis processes is shown in Fig. 1. Fig. 1 (a) presents the steps of the synthesis of C-mCS/GO, in which, initially, magnetic chitosan (mCS) is prepared using glutaraldehyde as a crosslinking agent, followed by the preparation of the composite C-mCS/GO using DCC and DMAP. Fig. 1 (b) shows the synthesis of G-mCS/GO, in which CS, GO and G-Fe$_3$O$_4$ are crosslinked using proanthocyanidin. The synthesis methodology of C-mCS/GO and G-mCS/GO is described in detail in sections 2.2.1. to 2.2.6.

2.2.1. Preparation of graphene oxide (GO)

The synthesis of GO was performed by the modified Hummers method (1958) using preoxidized graphite according to the methodology reported by Prediger et al. (2018). Initially, the preparation of preoxidized graphite was carried out by adding 20 g of mineral graphite, 120 mL of H_2SO_4, 10 g of K_2SO_4 and 10 g of P_2O_5 in a beaker in an ice bath with magnetic stirring. When the system reached room temperature, it was heated at 80 °C for 6 h. When it reached room temperature, the solution was added dropwise to a beaker containing 1 L of ultrapure water, and the system was placed in an ice bath with magnetic stirring. The obtained mixture was washed with ultrapure water to reach pH 6.

For the synthesis of GO, by the modified Hummers method (1958), the preoxidized graphite was added to an Erlenmeyer flask containing 500 mL of concentrated H_2SO_4 under magnetic stirring and an ice bath. Then, 10 g of $NaNO_3$ was slowly added to the system, and after 2 h, 60 g of $KMnO_4$ was added to the medium. The system was kept reacting at 0 °C for 1 h and then kept reacting at 25 °C for 7 days. After that, the system was cooled in an ice bath, and then 2 L of ultrapure water and 100 mL of aqueous H_2O_2 (3% v/v) were added. The system was heated at 100 °C for 30 min and then cooled and placed in a conical tube, which was subjected to centrifugation at 8000 rpm for 5 min. In a centrifuge system, the precipitate obtained was washed with 10 L of a 3% H_2SO_4 and 0.5% H_2O_2 solution. Then, the material was washed with a 10% HCl solution and, finally, washed with ultrapure water to reach pH 5. After the washing steps, the material obtained was stored in dialysis bags, which were immersed in ultrapure water to remove the salts present in the material. The immersion water was changed and monitored over time until the conductivity value was equal to the characteristic conductivity of ultrapure water. The material obtained was diluted in ultrapure water and submitted to an ultrasound bath for 1 h to form GO.

2.2.2. Conventional synthesis of Fe$_3$O$_4$ magnetic particles

The conventional synthesis of magnetic iron particles (C–Fe$_3$O$_4$) was performed based on the methodology reported by Silva et al. (2013). Initially, 600 mL of water, 60 mL of iron(II) chloride solution (0.6 M), 60 mL of iron(III) chloride solution (1.1 M) and 3 mL of oleic acid were added to a volumetric flask under magnetic stirring and ambient atmosphere. Then, NH_4OH was added dropwise to the system until it reached pH 11. When the mixture reached pH 11, it was heated at 85 °C for 30 min, washed with ultrapure water and filtered in a Büchner funnel until reaching pH 7. The material was dried in an oven at 100 °C for 48 h.

2.2.3. Conventional synthesis of magnetic chitosan (mCS)

The conventional synthesis of magnetic chitosan (mCS) was performed based on the methodology reported by Wang et al. (2016). Initially, 3 g of chitosan (CS) was dissolved in a 2% CH_3COOH solution in a 1 L volumetric flask. The system was kept under strong agitation for 2 h, followed by an ultrasound bath for 10 min. After that, 6.5 g of Fe$_3$O$_4$ magnetic particles were added under mechanical agitation. The system obtained was subjected to an ultrasonic bath for 10 min and then
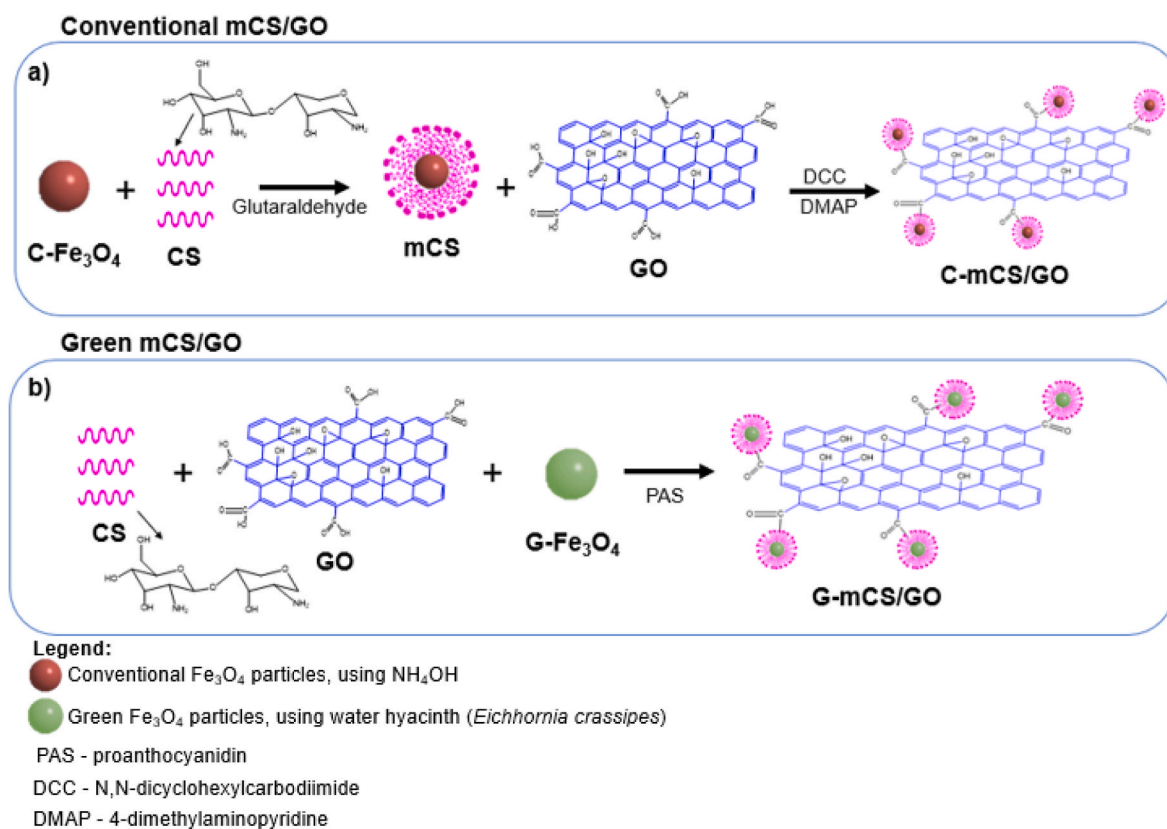
Fig. 1. Schematic diagram of the synthesis of a) C-mCS/GO and b) G-mCS/GO.

subjected to mechanical agitation for 1 h. After that, 200 mL of mineral oil was slowly added to the mixture, and the system was kept under mechanical agitation for 30 min. Then, 30 mL of glutaraldehyde was added to the system, which was subjected to mechanical agitation for 1 h. The mixture obtained was placed in a beaker containing a solution of NaOH (1 M) and stirred for 1 h. The material obtained was filtered with petroleum ether, subjected to a 5 min ultrasound bath, washed with ethanol and subjected to a 5 min ultrasound bath. After the ultrasound bath, the material was washed with ultrapure water to reach pH 7. Finally, it was dried at 100 °C for 48 h in an oven.

2.2.4. Conventional synthesis of mCS/GO

The conventional synthesis of mCS/GO (C-mCS/GO) was performed according to the adapted methodology reported by Maleki and Paydar (2015). In a volumetric flask, flamed, 2.3 g of GO and 300 mL of DMF were added under a nitrogen atmosphere and magnetic stirring. The mixture was subjected to magnetic stirring for 2 h, followed by an ultrasound bath for 1 h. After that, 20.7 g of DCC and 13.8 g of DMAP were placed into the mixture under a nitrogen atmosphere at 25 °C. The system was subjected to magnetic stirring for 48 h. The material obtained was submitted to a filtering step in a Büchner funnel with an aqueous solution of CH_3COOH (2%) to remove the extra CS. Then, the filtrate was subjected to an ultrasonic bath for 10 min. Subsequently, the material obtained was subjected to a sequential washing step with ultrapure water, methanol, acetone and ultrapure water. Finally, the product obtained was dispersed in water, placed in an amber glass bottle, and kept in the refrigerator.

2.2.5. Green synthesis of Fe₃O₄ magnetic particles

The green synthesis of magnetic iron particles (G-Fe_3O_4) was performed based on the adapted methodology reported by Zhang et al. (2021). Initially, the water hyacinth (*Eichhornia crassipes*) leaves were washed, dried at room temperature and ground to prepare the leaf

extract. Then, a solution of $FeCl_2.4H_2O$ and $FeCl_3.6H_2O$ (2 M) with a molar ratio of 2 Fe^{3+}:1 Fe^{2+} was prepared. Subsequently, 100 mL of water hyacinth extract and 3 mL of oleic acid were added to the solution. The mixture was subjected to magnetic stirring for 2 h, and then an aqueous solution of NaOH (1 M) was added dropwise until it reached pH 7. The mixture was stirred for 1 h at 55 °C, and then an aqueous solution of NaOH (2 M) was added dropwise until it reached pH 11. It was subjected to strong magnetic stirring for 30 min. The material obtained was washed with ethanol and then with ultrapure water to reach pH 7. The material obtained was dried for 48 h in an oven.

2.2.6. Green synthesis of mCS/GO

The green synthesis of mCS/GO (G-mCS/GO) followed the adapted methodology reported by Santos et al. (2020). In a volumetric flask, 3 g of CS was dissolved in 625 mL of ultrapure water under ambient atmosphere and strong magnetic stirring for 1 h. Subsequently, the system was placed in an ultrasound bath for 1 h and again kept under strong magnetic agitation for 1 h. Then, 2.5 g of dried GO was added to the homogeneous mixture. It was kept under magnetic stirring for 1 h, followed by an ultrasound bath for 1 h and again subjected to strong magnetic stirring for 8 h. After that, 6 g of green Fe_3O_4 magnetic particles were added to the system under strong magnetic stirring for 6 h. After that, the content of the volumetric flask was transferred to a beaker, and the system was subjected to mechanical agitation (150 rpm). Then, 6 g of PAS was added to the system under ambient atmosphere and mechanical agitation for 2 h. Subsequently, the material obtained was submitted to a washing step with ultrapure water and then dispersed in water, placed in an amber glass bottle, and kept in the refrigerator.

2.3. Characterization analyses

Table 1 presents the analytical techniques applied for the

Table 1

Characterization analysis of C-mCS/GO and G-mCS/GO composites.

Technique	Equipment	Procedure
X-ray diffraction (XRD)	Shimadzu XRD7000, Japan	Vacuum dried at 130 °C for 12 h. Cu Kα radiation with λ = 0.154 nm, operating at 40 kV and 30 mA, at 25 °C.
X-ray photoelectron spectroscopy (XPS)	XPS spectrometer (ScientaOmicron ESCA+) with a high-performance hemispheric analyzer (EAC2000). The analysis of the XPS spectra was realized by using the CASA XPS software.	Al Kα (h ν = 1486.6 eV) radiation as the excitation source, 10^{-9} Pa. The XPS high-resolution spectra were recorded at constant pass energy of 20 eV with a 0.05 eV per step.
Fourier transform infrared spectroscopy (FTIR)	Thermo Scientific equipment (Nicolet 6700, Madison/USA).	KBr method, range 4000–400 cm^{-1}, resolution 4 cm^{-1}, and scan 32.
Magnetization curves	Vibrating sample magnetometer (VSM)	Function of a magnetic field (Oe), at room temperature.
Scanning Electron Microscopy (SEM) and Energy Dispersive X-ray Spectroscopy (EDS)	Jeol model J6360 LV	A drop of the suspension containing the composites was placed on a silicon wafer and vacuum dried.
Thermogravimetric analysis (TG/DTG)	DTG-60, Shimadzu, Japan	N_2 atmosphere and flow of 50 mL min^{-1}, from 25 °C to 1000 °C with heating rate of 10 °C.min^{-1}.
Zeta potential (mV)	Zetasizer Nano ZS ZEN3600 (Malvern)	$C_0 = 0.001$ mg mL^{-1}, at 25 °C. The pH of the suspensions (4, 6, 8, 10) were adjusted by adding HCl and NaOH solutions.

characterization of the composites C-mCS/GO and G-mCS/GO.

2.4. Molecular modeling

Molecular modeling was applied to describe the chemical structures and establish quantitative relationships between the physicochemical properties of PAH molecules (naphthalene, anthracene and fluoranthene). Through molecular modeling, it is possible to perform theoretical functional density (DFT) calculations, thus aiming to detail the geometric properties, as well as calculate the quantum chemical molecular descriptors of the PAHs, which include the HOMO - highly occupied molecular orbital energy (E_H), LUMO - lowest unoccupied molecular orbital energy (E_L) and chemical energy change (Δ_{HL}).

The electronic chemical potential (μ), global chemical hardness (η) and the general electrophilicity index (ω) values can be calculated from the values of E_H and E_L, according to Equations (1)–(3):

$$\mu = \frac{-(E_H + E_L)}{2} \tag{1}$$

$$\eta = \frac{(-E_H + E_L)}{2} \tag{2}$$

$$\omega = \frac{\mu^2}{2\eta} \tag{3}$$

The chemical structures of the PAHs were designed by using ChemDraw® software (version 16), and then the 3D molecular structures were designed by using Avogadro® software (version 1.2.0). The quantum chemical descriptors and the minimum energy geometry of the

PAHs were analyzed by using DFT calculations implemented in the Gaussian® software (version 09). DFT calculations were performed by Beck's theoretical model, 3-parameter, Lee-Yang-Parr correlation (B3LYP) and as base set 6-31G (d) and 6-31G (d,p), which are used to optimize the molecular geometry of organic molecules, such as PAHs, to obtain a stable molecular structure, as well as to minimize the system energy.

From the optimized geometry of the molecules obtained through Avogadro®, calculations were performed in Gaussian® by using the B3LYP model and the 6-31G (d) and 6-31G (d,p) polarization functions, aiming to determine if the obtained geometry is stable. For calculation purposes, the effect of water as a solvent was taken into account for the simulations. The HOMO (E_H) and LUMO (E_L) molecular orbitals were also obtained through Avogadro® by using the Test file from the Gaussian® directory. The electrostatic potential map of the PAHs was obtained through Avogadro®, applying the van der Waals model as the 'Surface type'.

2.5. Adsorptive affinity assays

The adsorptive assays were carried out in triplicate to evaluate the affinity of the PAHs (naphthalene, anthracene and fluoranthene) for the adsorbents (conventional and green mCS/GO). Initially, synthetic stock solutions were prepared at 10 mg. L^{-1} by dissolving naphthalene in methanol (4% CH_3OH/96% H_2O), anthracene in acetonitrile (30% C_2H_3N/70% H_2O) and fluoranthene in acetonitrile (15% C_2H_3N/85% H_2O), which were stored in an amber glass bottle and kept in the refrigerator. The working solutions of naphthalene, anthracene and fluoranthene used in the affinity assays were prepared from dilutions of the PAH stock solutions at 0.01 mmol. L^{-1} (1.28, 1.78 and 2.02 mg. L^{-1}, respectively).

The adsorption experiments were performed in a batch system in a shaker (Jeio Tech, SI-600R, South Korea) in triplicate with stirring at 200 rpm at 25 °C ± 1 °C for 30 min to reach adsorption equilibrium. To evaluate the affinity of PAHs for the adsorbents over the time of the experiment, a dosage of adsorbent of 0.1 mg mL^{-1} was used. After the adsorption processes, the adsorbents were removed by magnetic separation, and then the materials were centrifuged under stirring at 6000 rpm for 15 min.

The residual concentration of naphthalene in synthetic wastewater was measured using a high-performance liquid chromatography system (HPLC) (Shimadzu), which consists of a CTO-10ASVP heating oven, SPD-10AV UV–Vis detector, LC-10AD gradient pump and CBM-10A connection module. The HPLC system was equipped with a C18 column (5 μ, 150 mm × 4.6 mm) (Phenomenex, Torrance, USA) with a 25 μL manual sample injector, and the chromatographic data obtained were processed using LC Solution software. The mobile phase consisted of 85% methanol and 15% deionized water at a flow rate of 1 mL min^{-1}, wavelength set at 254 nm and column temperature of 25 °C. Before injecting the samples into the HPLC system, they were filtered with a PTFE syringe filter (0.45 μm) to completely remove the adsorbent particles from the system. The residual concentrations of anthracene and fluoranthene in synthetic wastewater were measured by a UV–vis spectrophotometer (Shimadzu/UV-1900) using the absorption peaks set at 251 nm and 236 nm for anthracene and fluoranthene, respectively. More information regarding the PAH calibration curves is described in the Supplementary Material (see Table S1).

The removal efficiency (%Rem) and adsorption capacity (q(t)), in mmol.g^{-1}, were calculated using equations (4) and (5), respectively:

$$\%Rem = \frac{(C_0 - C_f)}{C_0} \cdot 100 \tag{4}$$

$$q(t) = \frac{(C_0 - C_f)}{m} \cdot V \tag{5}$$

where C_0 is the initial PAH concentration (mmol. L^{-1}), C_f is the concentration of PAHs after the adsorption process (mmol. L^{-1}), V is the volume of the solution (L) and m is the adsorbent mass (g).

3. Results and discussion

3.1. Conventional and green mCS/GO characterizations

3.1.1. Evaluation of the crystal structure of synthesized materials

The diffractograms of the composites are shown in Fig. 2 (a). Conventional and green Fe_3O_4 (C–Fe_3O_4 and G- Fe_3O_4, respectively) particles showed diffraction peaks at 30.3°, 35.5°, 43.4°, 57.3°, and 62.9°, corresponding to the crystallographic planes (2 2 0), (3 1 1), (4 0 0), (5 1 1) and (4 4 0), respectively. The results confirm the obtainment of Fe_3O_4 particles in cubic form, as reported in the literature (Neves et al., 2020; Shi et al., 2020). Through the diffraction patterns, it was not possible to observe the presence of the peaks at 21° and 33°, corresponding to the planes (1 1 0) and (1 0 4), respectively, which indicates that the Fe_3O_4 particles are not present in their composition goethite [α-Fe^{3+}O(OH)] and hematite (Fe_2O_3) (Solano et al., 2021). The average crystal sizes were determined by Debye-Scherrer's equation (D = $K\lambda \bullet (\beta cos\theta)^{-1}$), where D is the crystal size (nm), K is the Debye-Scherrer's constant (0.94), λ is the wavelength (0.15406 nm), β is the maximum width of the highest intensity peaks at half height and θ is the diffraction angle. The average crystal sizes of the C–Fe_3O_4 and G-Fe_3O_4 particles, taking into account the highest intensity peaks, were 7.2 and 13.2 nm, respectively.
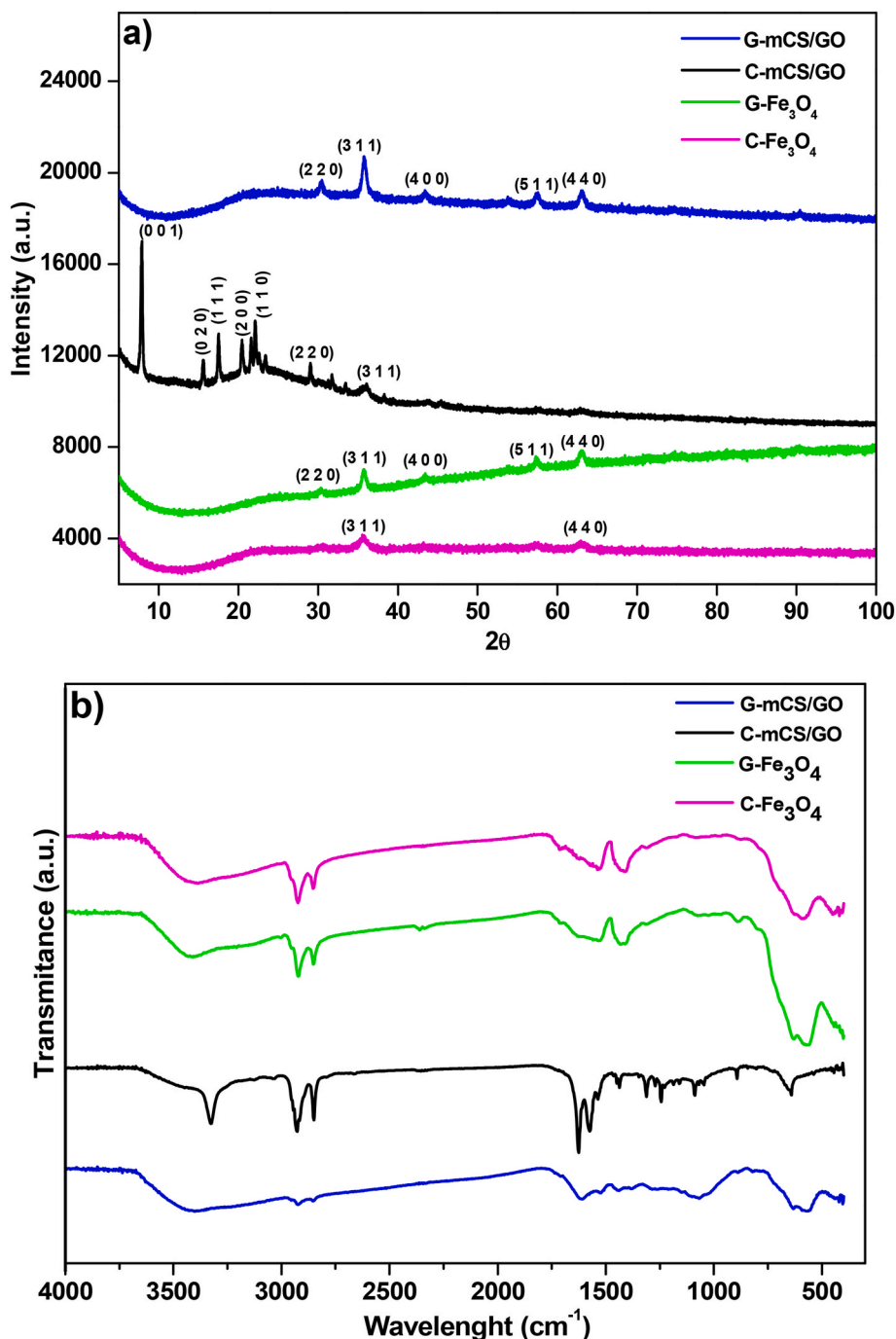

Fig. 2. a) XRD diffractograms and b) FT-IR spectrum of G-mCS/GO (blue line); C-mCS/GO (black line); G-Fe_3O_4 (green line) and C–Fe_3O_4 (pink line).

The XRD diffractogram of C-mCS/GO indicated the presence of a greater intensity peak at 7.9°, referring to the crystallographic plane (0 0 1) of GO, with an interplanar distance of 1.28 nm, calculated according to Bragg's equation. In the literature, GO shows a peak at approximately 10°, and this shift may be associated with the incorporation of mCS, thus increasing the repulsion between the GO nanosheets. It is also possible to observe the presence of a peak at 22.3°, referring to the crystallographic plane (1 1 0), which is associated with the presence of mCS (Neves et al., 2020). Furthermore, characteristic peaks of Fe_3O_4 particles in their dominant cubic form were observed in the XRD pattern of both composites (Prediger et al., 2018; Neves et al., 2020).

3.1.2. Functional group identification

The FT-IR spectra of the composites are shown in Fig. 2 (b). The C-Fe_3O_4 and G-Fe_3O_4 spectra showed the presence of two bands at 2920 and 2850 cm^{-1}, which are associated with the stretching vibrations of the $-CH_2-$ groups, attributed to the presence of oleic acid and water hyacinth extract in the synthesis of Fe_3O_4 particles (Silva et al., 2013). The bands at 1470 and 570 cm^{-1} can be associated with the stretching vibration of the Fe–O bond, thus indicating the presence of magnetite (Zhang et al., 2021).

The spectrum of C-mCS/GO showed a peak at 3330 cm^{-1}, which corresponds to the stretching vibrations of the N–H and O–H groups (Gul et al., 2016). Furthermore, it is possible to verify that C-mCS/GO and G-mCS/GO showed peaks at 2920, 2850 and 645 cm^{-1}, which are attributed to the presence of Fe_3O_4 magnetic particles (Wang et al., 2015). The peak at 1620 cm^{-1} is associated with stretching vibrations of the C=O groups, which can be attributed to the presence of –COOH groups and can also be associated with the presence of residual amide groups attributed to CS (Travlou et al., 2013; Tang et al., 2021). Finally, the peaks at 1070 and 1230 cm^{-1} correspond to the stretching vibrations of the C–O and –COOH groups, respectively (Neves et al., 2020).

3.1.3. Evaluation of chemical composition and functional groups

Through XPS analysis, the chemical composition of the composites, the nature of their functional groups, and the sp^3 and sp^2 components of the carbon atoms were determined (Prediger et al., 2018). Fig. S1 (a) and (b) present the survey spectra of the C-mCS/GO and G-mCS/GO samples, respectively. Both survey spectra show characteristic peaks of GO, such as C (1 s) at 285.7 eV and O (1 s) at 531.3/530.2 eV. The survey also shows peaks related to N(1 s) at 400.2/400.8 eV and Fe (2p) peaks at 711.2/711.3 eV and 723.6/725.4 eV, associated with the incorporation of CS and the presence of Fe_3O_4, respectively, in the structures of C-mCS/GO and G-mCS/GO (Li et al., 2017; Neves et al., 2020). The elemental composition (%) of C, O, N and Fe for both materials calculated from XPS analysis is shown in Table 2. The Fe content in G-mCS/GO is higher (3.5%), as well as its oxygen content (26.3%) when compared to C-mCS/GO, which is associated with a better incorporation of Fe_3O_4 particles, thus indicating a greater magnetic potential of this material when compared to the conventional one.

The high-resolution XPS spectrum of C-mCS/GO for C (1s) (Fig. 3a) revealed the presence of five peaks centered at 284.5, 285.3, 286.8, and 288.3 eV, which correspond to C–C/C–H (50.3%), C–N/C–OH (29.5%), C–O (13.3%, hydroxyl and epoxy) and (C=O) (6.9%), respectively (Neves et al., 2020). The high-resolution XPS for O (1s) (Fig. 3c) indicated the presence of three peaks at 530.6, 532.1, and 533.2 eV, attributed to the functional groups containing oxygen Fe–O (38.8%),

C–OH/C=O (33.6%) and O–C–O (27.6%) (Tang et al., 2021). Regarding nitrogen, the high-resolution N (1s) spectrum (Fig. 3e) showed the presence of peaks at 399.1 and 400.5 eV, which are associated with the nitrogenous functional groups C–NH_2 (75.7%) and (C=O)–N (24.3%), thus indicating the presence of chitosan in the structure (Zuo et al., 2013; Francisco et al., 2015). In the high-resolution Fe (2p) spectrum (Fig. 3g), the peaks at 711.4 and 724.6 eV, associated with Fe 2p $_{3/2}$ and Fe 2p $_{1/2}$, respectively, indicate the formation of Fe_3O_4 (Wang et al., 2015).

The high-resolution XPS spectrum of G-mCS/GO for C (1s) (Fig. 3b) confirmed the presence of four peaks centered at 284.6, 285.8, 286.9, and 288.5 eV, which correspond to C–C/C–H (54.1%), C–N/C–OH (28.8%), C–O (8.7%) and C=O (9.0%), respectively [24]. The high-resolution XPS for O (1s) (Fig. 3d) indicated the presence of three peaks at 530.2, 532.1, 533.1 eV, attributed to the functional groups containing oxygen Fe–O (32.1%), C–OH/C=O (35.6%) and O–C–O (32.2%) (Neves et al., 2020). Regarding nitrogen, the high-resolution N (1s) spectrum (Fig. 3f) showed the presence of peaks at 399.5 and 401.9 eV, which are associated with the nitrogenous functional groups C–NH_2 (78.9%) and NH_3^+ (21.1%, protonated amine groups), thus indicating the presence of chitosan in the structure of the material (Francisco et al., 2015; Zhang et al., 2019). In the Fe (2p) high-resolution spectrum (Fig. 3h), the peaks at 711.1 and 724.9 eV, associated with Fe 2p $_{3/2}$ and Fe 2p $_{1/2}$, respectively, indicate the formation of Fe_3O_4 (Tang et al., 2021).

3.1.4. Magnetization curves

Fig. 4 shows the C-mCS/GO and G-mCS/GO magnetization curves. The results indicated that C-mCS/GO and G-mCS/GO show superparamagnetic properties at room temperature, as the magnetization curves obtained do not exhibit coercivity, which indicates that they can be removed from a suspension with a permanent magnet (Zhang et al., 2021).

The calculated saturation magnetization values were 26 emu/g and 7.5 emu/g for G-mCS/GO and C-mCS/GO, respectively. This decrease may be related to the methodology applied for the synthesis of Fe_3O_4 magnetic particles, since in the green protocol, water hyacinth extract was used, which is rich in polyphenols, acting as a stabilizing agent for the iron particles (Shi et al., 2020). This decrease can also be associated with the type of crosslinking agent applied in the synthesis of mCS/GO, glutaraldehyde for the conventional synthesis and PAS for the green synthesis. Comparing the results of C-mCS/GO and G-mCS/GO, it is observed that PAS had a better action as a crosslinking agent, which allowed a greater incorporation of G-Fe_3O_4 particles into the material, thus generating an increase in the value of saturation magnetization of G-mCS/GO (Neves et al., 2020; Shahraki et al., 2020).

3.1.5. Evaluation of morphological properties of synthesized materials

The micrographs of the composites were determined by SEM and are shown in Fig. 5(a–f). Fig. 5(a–d) shows the micrographs of C-mCS/GO and G-mCS/GO, in which the morphologies were verified in the form of two-dimensional layers with a wrinkled surface, similar to crushed sheets, which are typical of materials containing GO (Jiang et al., 2016; Song et al., 2021). Furthermore, it is possible to observe spherical Fe_3O_4 particles well distributed on the surface of the composites, which can be associated with the presence of hydrogen bonds between the Fe_3O_4 particles and the functional groups present on the surface of GO (Sheshmani et al., 2014). Fig. 5(e and f) shows micrographs of the aggregated Fe_3O_4 magnetic particles, which are associated with the van der Waals interactions between Fe_3O_4 (Neves et al., 2020).

The chemical elements identified through EDS and SEM analyses, as well their mass compositions (%), are shown in Table 3. The difference in N composition values between the XPS and EDS analyses can be attributed to differences in the analytical techniques, since EDS analysis is a semiquantitative technique and, therefore, has its limitations. By EDS analysis, the Fe_3O_4 magnetic particles have chemical elements C, O

Table 2
The elemental composition (%) of C, O, N and Fe by XPS analysis.

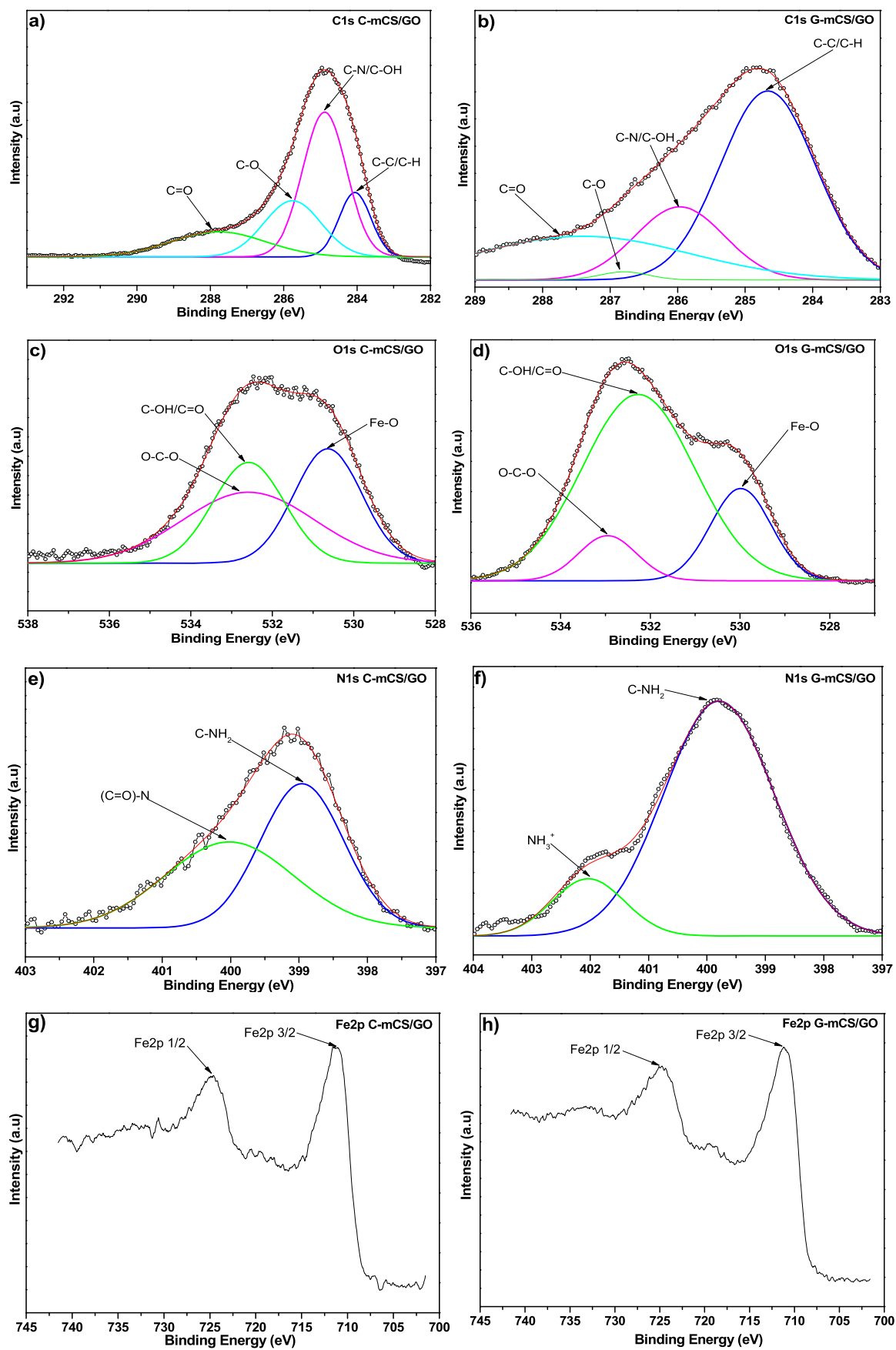| Elements	C-mCS/GO	G-mCS/GO
C (1s)	79.3	69.3
O (1s)	14.1	26.3
N (1s)	4.9	0.9
Fe (2p)	1.7	3.5

Fig. 3. High-resolution of C (1s) (a–b); O (1s) (c–d); N (1s) (e–f) and Fe (2p) (g–h).
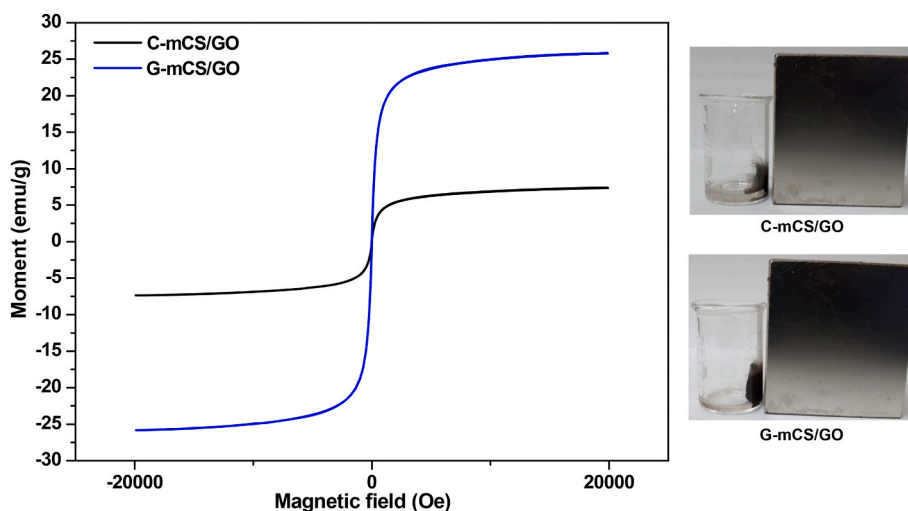
Fig. 4. Magnetization curves of C-mCS/GO and G-mCS/GO.

and Fe. The presence of C in the Fe_3O_4 magnetic particles is associated with the presence of oleic acid, which is used as a stabilizing agent in the conventional protocol to prevent particle aggregation. For the $G-Fe_3O_4$ particles, the presence of C is associated with the polyphenols present in the water hyacinth extract, used as a stabilizing agent in the green protocol (Shi et al., 2020).

The C-mCS/GO and G-mCS/GO composites contained the chemical elements C, N, O and Fe. In both composites, the nitrogen detected in the EDS analysis is associated with the amine functional groups present in CS (Subedi et al., 2019). The mass composition of Fe in G-mCS/GO is greater than that in C-mCS/GO, in accordance with the results obtained through XPS analyses, which is associated with its higher saturation magnetization when compared to that of the conventional composite. This increase can be associated with the crosslinking agent PAS used in the green synthesis process, which enables greater crosslinking of the Fe_3O_4 particles, preventing their leaching into the medium during the washing step and providing excellent magnetic properties to G-mCS/GO (Shi et al., 2020).

3.1.6. Evaluation of the thermal properties of adsorbents

The thermogravimetric curves of C-mCS/GO and G-mCS/GO obtained through TG/DTG analysis are shown in Fig. 6(a and b). Through the thermogravimetric curve of C-mCS/GO (Fig. 6a), it is observed that the mass loss occurs through three stages. In the first stage, the temperature ranged from 26 to 139 °C, with a mass loss of 1.56%, referring to the evaporation of water adsorbed on the surface of the material. The second stage, which occurs between 139 and 262 °C, has a mass loss of 52.92%, which is attributed to the decomposition of oxygenated functional groups such as carbonyls, hydroxyls, epoxides, carboxylic acids and nitrogen oxides. Between 262 and 645 °C, the third stage was observed with a mass loss of 24.99%, which is associated with mCS decomposition (Ganguly et al., 2011; Gul et al., 2016). Through DTG analysis, a major mass loss was observed with an exothermic signal at approximately 200 °C, which is associated with the decomposition of oxygenated species, thus generating the formation of byproducts such as CO, CO_2 and steam (Guo et al., 2012).

Through the thermogravimetric curve of G-mCS/GO (Fig. 6 (b)), it can be observed that the mass loss occurs through two distinct stages. The first stage is verified between 26 and 131 °C, showing a mass loss of 4.68%, referring to the evaporation of water adsorbed on the surface of the material. The second stage, which occurs in the temperature range from 131 to 642 °C, with a mass loss of 60.24%, is associated with the decomposition of functional groups containing oxygen, as well as the decomposition of mCS. Through DTG analysis, it is observed that the major mass loss occurs at approximately 300–400 °C, which is

associated with the pyrolyzis processes of the oxygenated functional groups, thus generating CO, CO_2 and steam. Through this analysis, it can also be observed that the thermal decomposition of mCS/GO produces the release of gases, thus generating a thermal expansion of the material, which can be confirmed by the major mass loss at this stage. The results indicate that the green composite presents greater stability to thermal degradation than the conventional composite since its decomposition occurs at higher temperatures (Stankovich et al., 2007; Gul et al., 2016).

3.1.7. pH evaluation

Zeta potential (mV) is a very important factor for determining the magnitude and sign of the surface charge of a colloidal suspension, thus aiming to evaluate its stability and electrostatic interactions between nanomaterials in this suspension (Yang et al., 2010). Fig. 6c shows the zeta potential (mV) for C-mCS/GO and G-mCS/GO at different pH values (4, 6, 8, 10). Zeta potential measurements indicated that, for the evaluated pH range, both nanomaterials had negative values. C-mCS/GO presented more negative zeta potential values for all pH ranges, indicating that the suspension of nanomaterials is more stable, even under acidic conditions (Gurunathan et al., 2014). The G-mCS/GO zeta potential values also indicate the presence of a less negatively charged nanomaterial, which may be associated with the presence of protonated functional groups from the $G-Fe_3O_4$ particles (Fe^{2+} and Fe^{3+}), since XPS results indicated a higher content of iron in G-mCS/GO. This increase may be attributed to the performance of the crosslinking agent (PAS) used in the synthesis process of the green adsorbent (Han et al., 2012; Kalliola et al., 2017).

3.2. Molecular simulation

Through the molecular simulations performed by using ChemDraw® and Avogadro® software, information on the physicochemical and geometric properties of PAHs was obtained. Table 4 shows the physicochemical properties of the naphthalene, anthracene and fluoranthene molecules calculated by ChemDraw® and Avogadro® software.

Fig. 7 shows the chemical structures, optimized geometry and electrostatic potential of PAH molecules (naphthalene, anthracene and fluoranthene) obtained by using ChemDraw®, Avogadro® and GaussView® software. The optimization of the isolated PAHs was performed through the B3LYP method, with 6-31G (d) and 6-31G (d,p) as the basis set. Fig. S2 shows the lowest molecular energies of the optimized PAH geometries, so that the most stable conformers, that is, the lowest energies, were obtained by the 6-31G (d,p) base set. Additional stability and vibrational frequency calculations were performed to ensure that the structures are stable and that they correspond to the
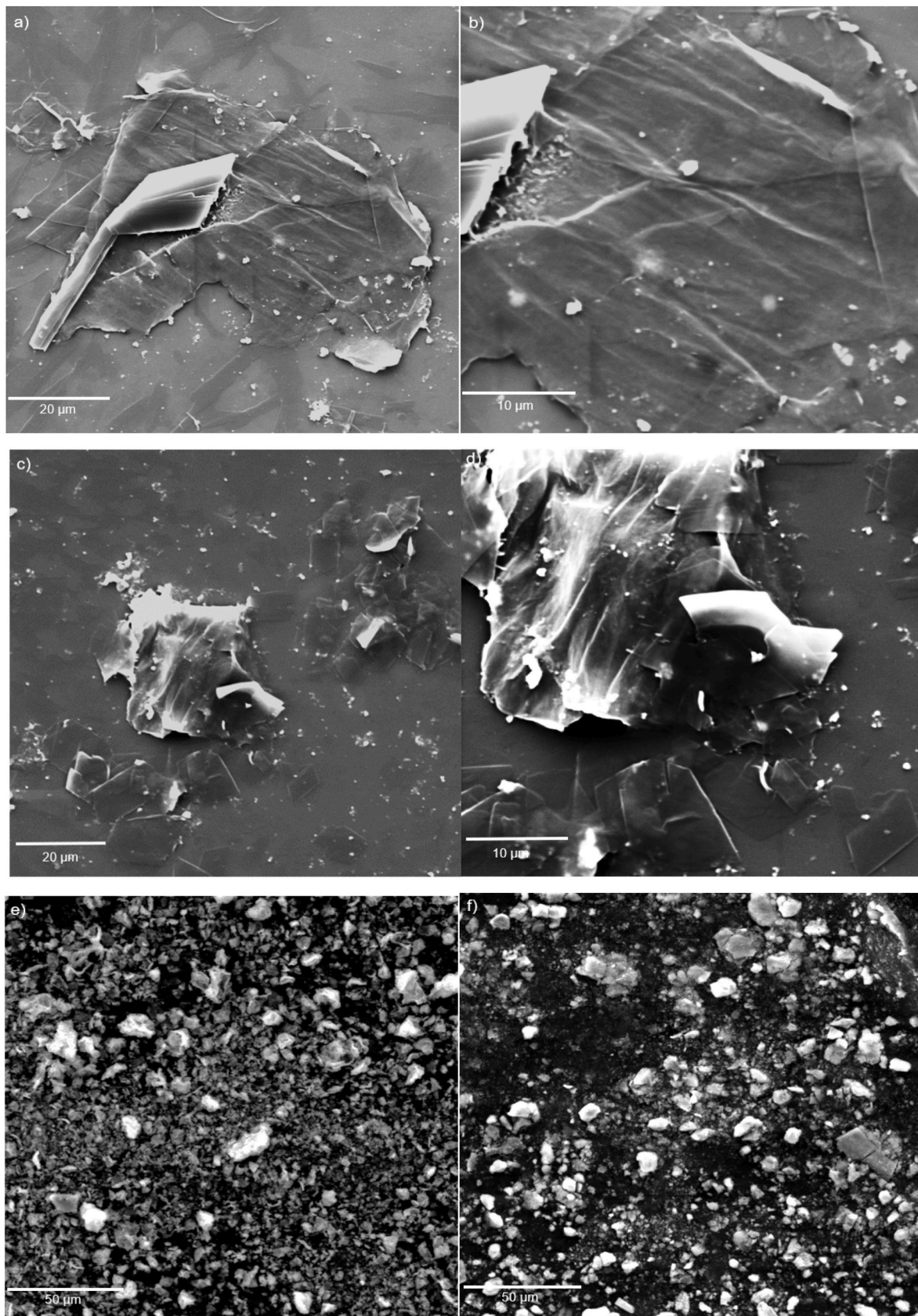
Fig. 5. SEM micrographs of C-mCS/GO a) 2000x, b) 5000× magnification; G-mCS/GO c) 2000x, d) 4500× magnification; e) C–Fe$_3$O$_4$, and f) G-Fe$_3$O$_4$.

Table 3

Elemental mass composition (%) of C-mCS/GO and G-mCS/GO and C–Fe_3O_4 and G-Fe_3O_4 particles.

Mass composition (%)				
Elements	C-mCS/GO	G-mCS/GO	C–Fe_3O_4	G-Fe_3O_4
C	53.17	45.32	14.22	12.55
N	26.45	19.88	–	–
O	18.91	25.95	27.47	21.30
Fe	1.47	8.84	57.60	66.15

minimum energy settings (Salter and Foresman, 1998). Tables S2-S4 show the optimized bond lengths of the PAH molecules, where the bond lengths represent the distance between the center of the two bonded atoms.

The naphthalene, anthracene and fluoranthene molecules have their largest dimensions of 7.201 Å, 9.546 Å and 9.045 Å, respectively, as shown in Fig. 7. The electrostatic potential map of the PAH molecules, calculated by GaussView 5® software, is also shown in Fig. 7, which provides information about the distribution of electron density. The electrostatic potential map indicates the electron distribution in each region of the PAH molecules, where the blue color represents the electron-poor regions and the red color represents the electron-rich regions (Mishra and Yadav, 2012; Santos et al., 2014).
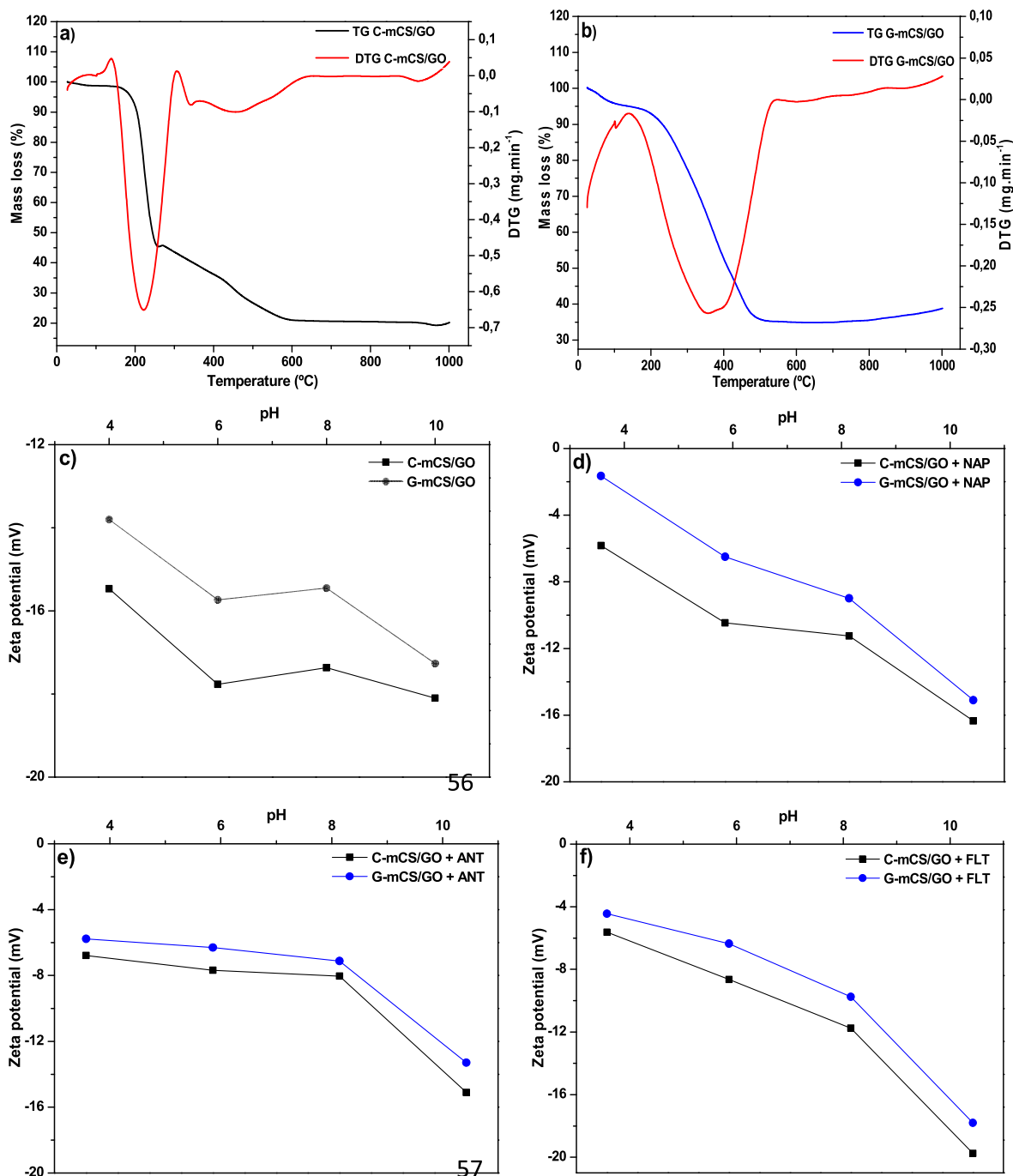

Fig. 6. TG/DTG curves and zeta potential for (a–c) C-mCS/GO and (b–c) G-mCS/GO and the zeta potential in suspension with (d) naphthalene, (e) anthracene, and (f) fluoranthene solutions.

Table 4

Physicochemical properties of naphthalene, anthracene and fluoranthene molecules.

Properties	Naphthalene	Anthracene	Fluoranthene
Molecular formula	$C_{10}H_8$	$C_{14}H_{10}$	$C_{16}H_{10}$
Molecular weight	128.171 g mol^{-1}	178.229 g mol^{-1}	202.251 g mol^{-1}
Melting point	261.08 K	351.38 K	425.42 K
Boiling point	474.06 K	589.54 K	651.56 K
Critical temperature	757.95 K	859.11 K	898.65 K
log K_{ow}[a]	3.37	4.54	5.22
Dipole Moment[b]	0 Debye	0 Debye	0.3291 Debye

[a] Mackay et al., 1992.
[b] Estimated through chemical modeling software Gaussian®.

Fig. 8 shows the HOMO and LUMO 3-D contours of naphthalene, anthracene and fluoranthene molecules. Table 4 presents the quantum chemical parameters obtained for the PAHs through the B3LYP/6-31G (d,p) model. The energy of the boundary orbitals (HOMO and LUMO) assessment is very important to understand the mechanisms involved in the adsorptive processes because through these quantum chemical descriptors, it is possible to delimit the regions in which molecules can donate (HOMO) or accept electrons (LUMO). The higher the HOMO is, the greater the electron donating capacity, and the lower the LUMO is, the easier it is to accept electrons. Through the HOMO and LUMO energy values presented in Fig. 8 and Table 5, it is possible to observe that ANT has a greater capacity to donate electrons than the other PAHs evaluated, while naphthalene has greater acceptance of electrons (Mishra and Yadav, 2012; Santos et al., 2014).

The difference between the HOMO-LUMO energies (gap) is important to indicate how stable the structure of the molecule is, so that the greater this difference is, the greater the stability of the molecule, and consequently, the lower its reactivity in chemical reactions. Based on the gap values shown in Fig. 8, naphthalene has a greater gap (4823 eV), which indicates greater stability and less reactivity, whereas anthracene has a smaller gap (3591 eV), thus indicating less stability and greater reactivity than naphthalene and fluoranthene (Umadevi and Sastry, 2011). According to the study by Naghavi et al. (2011), the gap depends on the molecular size, so this difference decreases as the PAH size increases, decreasing their stability.

HOMO and LUMO energies can also be used to calculate the quantum chemical parameters, according to Equations (1)–(3). μ measures the tendency of electrons to escape from the system (Parr and Pearson, 1983); η measures resistance to changes in electron density; in other words, it measures resistance to deformation, helping to determine the stability and reactivity of the molecule (Pearson, 1992); ω is an indicator of the ability to accept electrons (Parr et al., 1999).

Comparing the values of μ, η and ω for naphthalene, anthracene and fluoranthene, presented in Table 5, it is observed that FLT fluoranthene has a higher chemical potential, thus indicating a lower capacity to retain electrons; therefore, fluoranthene has less stability and greater reactivity than naphthalene and anthracene. Naphthalene is the hardest molecule, showing greater resistance to deformation in its electron density, while anthracene has less resistance to deformation. The value of the electrophilicity index indicates that fluoranthene is the strongest electrophile, with a greater tendency to accept electrons. Through the theoretical analysis of quantum chemical descriptors, it is concluded that anthracene and fluoranthene are the most reactive among the evaluated PAHs.

3.3. Adsorptive affinity assays

Through the adsorptive affinity assays, it was possible to evaluate the removal potential of PAHs (naphthalene, anthracene and fluoranthene) by the C-mCS/GO and G-mCS/GO adsorbents for a contact time of 30 min. The adsorption capacities (q(t)) of the PAHs by the adsorbents are shown in Table 6, and the removal efficiencies of the PAHs is shown in Fig. 9.

From the results presented in Fig. 9 and Table 6, it is observed that the best removal efficiency (%) and adsorption capacity (mmol.g^{-1}) were obtained by naphthalene for both C-mCS/GO and G-mCS/GO. The results also showed that the G-mCS/GO adsorbent was highly efficient for the removal of anthracene compared to the conventional adsorbent. These results show that G-mCS/GO is a potential adsorbent for PAH removal from wastewater. Table 7 shows a comparison of the adsorption and removal capacity of C-mCS/GO and G-mCS/GO for PAH adsorption with other materials presented in the literature.

When compared with conventional materials, green synthesized adsorbents are an alternative methodology to decrease the toxic effects associated with the excessive application of chemical products in conventional synthesis. In addition, the use of natural agents can be of great advantage for green synthesis processes due to the presence of active compounds, such as polyphenols and flavones, which can act as stabilizing and crosslinking agents. Such compounds can improve the properties of these green materials, boosting their performance in pollutant
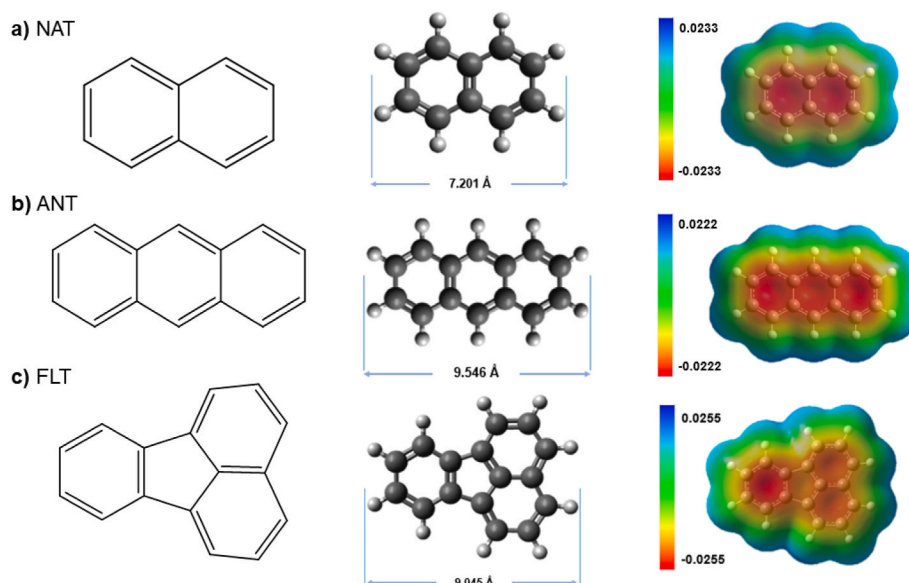

Fig. 7. Chemical structures, optimized geometry and electrostatic potential of PAH molecules: **a)** naphthalene; **b)** anthracene; **c)** fluoranthene.
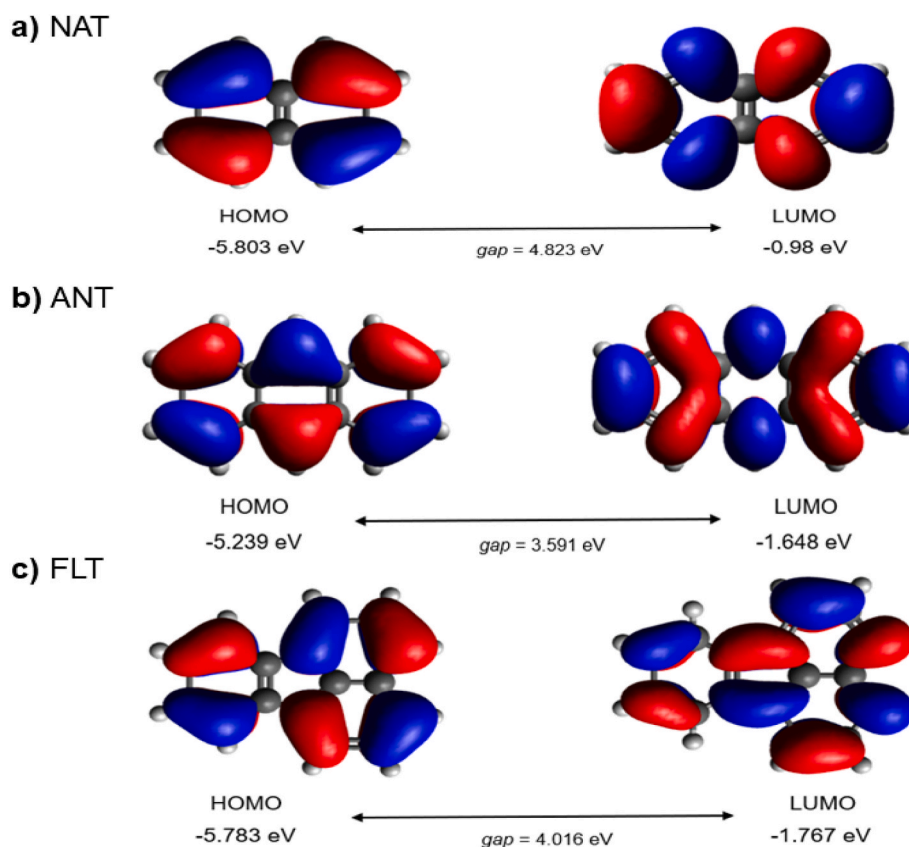
Fig. 8. 3-D contours of HOMO and LUMO: a) naphthalene; b) anthracene; c) fluoranthene (Positive Phase: Blue Color; Negative Phase: Red Color).

Table 5
Quantum chemical parameters of naphthalene, anthracene and fluoranthene using the B3LYP/6-31G (d,p) model.

Quantum chemical parameters	Naphthalene	Anthracene	Fluoranthene
HOMO energy (E_H, eV)	−5.803	−5.239	−5.783
LUMO energy (E_L, eV)	−0.980	−1.648	−1.767
Energy gap (Δ_{HL}, eV)	4.823	3.591	4.016
Chemical potential (μ, eV)	3.391	3.443	3.775
Chemical hardness (η, eV)	2.411	1.795	2.008
Electrophilicity index (ω, eV)	2.385	3302	3.548

Table 6
Adsorption capacity of PAHs by the adsorbents (C-mCS/GO and G-mCS/GO).

PAHs	Adsorption capacity ($mmol.g^{-1}$)	
	C-mCS/GO	G-mCS/GO
Naphthalene	0.094	0.093
Anthracene	0.048	0.089
Fluoranthene	0.076	0.062

adsorptive processes from wastewater (Shi et al., 2020; Zhang et al., 2021).

3.4. Mechanisms of PAH adsorption

The results obtained with the molecular simulation indicated that NAP molecules have greater stability than anthracene and fluoranthene molecules, which may contribute to increasing the π-π interactions between naphthalene molecules and the adsorbent surface (Li et al., 2018). Furthermore, the presence of oxygenated functional groups such as C=O and O–H in the structure of the adsorbents, as indicated in the
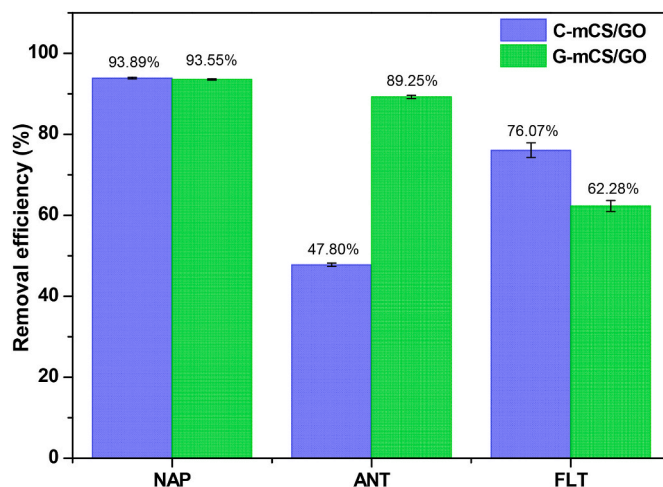

Fig. 9. Removal efficiency (%Rem) of PAHs (naphthalene, anthracene and fluoranthene). Conditions: $C_0 = 0.01$ mmol. L^{-1}, dosage of adsorbent of 0.1 mg mL^{-1}, 25 °C for 30 min.

FT-IR analyses (Fig. 2b), may be one of the factors that contribute to the presence of strong π-π interactions between the molecules of PAHs and the surface of the adsorbents (Song et al., 2021). Thus, the presence of these interactions can induce a greater adsorptive efficiency between PAHs and both C-mCS/GO and G-mCS/GO adsorbents. Fig. 10 illustrates the possible mechanisms involved in the naphthalene, anthracene and fluoranthene adsorption processes into G-mCS/GO.

Another mechanism that can contribute to PAH adsorption on the adsorbent surface is the hydrophobic effect. This effect is very important for the adsorption of nonpolar compounds, which contributes to

Table 7

Comparison of the adsorption capacity and removal efficiency of C-mCS/GO and G-mCS/GO with other adsorbents studied in the literature.

PAHs	Adsorbents	Experimental conditions	Adsorption capacity (mmol. g^{-1})	Removal efficiency (%)	References
Anthracene	Nitrogen-doped reduced graphene oxide (NRGO)	C_0: 0.0056 mmol.L^{-1}, 298 K, pH 7, 150 rpm, 48 h, D: 0.1 mg mL^{-1}	0.0324	58	[10]
Naphthalene	Thiourea-Magnetite-TiO_2 modified chitosan beads (Cs-T-M-Ti)	C_0: 0.078 mmol.L^{-1}, 298 K, pH 6.5, 200 rpm, 24 h, D: 0.5 mg mL^{-1}	0.067	–	[22]
Anthracene, Fluoranthene	Cetylpyridinium chloride (CPC)-MC; Didodecyldimethylammonium bromide (DDAB)-MC; Hexadecyltrimethylammonium bromide (HDTMA)-MC	C_0: 2.8×10^{-4} mmol.L^{-1} (ANT), C_0: 4.9×10^{-4} mmol.L^{-1} (FLT), 293 K, pH 6.5, 24 h, D: 1 mg mL^{-1}	ANT (4×10^{-3}, 4.1×10^{-3}, 4.2×10^{-3}) FLT (6.7×10^{-3}, 7.8×10^{-3}, 6.4×10^{-3})	Anthracene (61, 71, 65.6) Fluoranthene (52.5, 61.8, 44)	[50]
Fluoranthene	Lightweight expanded clay aggregate (LECA)	C_0: 9.9×10^{-5} mmol.L^{-1}, 298 K, pH 6.5, 300 rpm, 21 h, D: 2 mg mL^{-1}	3.5×10^{-5}	70.83	[51]
Naphthalene, Anthracene, Fluoranthene	C-mCS/GO	C_0: 0.01 mmol.L^{-1}, 298 K, pH 6.5, 200 rpm, 30 min, D: 0.1 mg mL^{-1}	0.094, 0.048, 0.076	93.89, 47.80, 76.07	This study
Naphthalene, Anthracene, Fluoranthene	G-mCS/GO	C_0: 0.01 mmol.L^{-1}, 298 K, pH 6.5, 200 rpm, 30 min, D: 0.1 mg mL^{-1}	0.093, 0.089, 0.062	93.55, 89.25, 62.28	This study
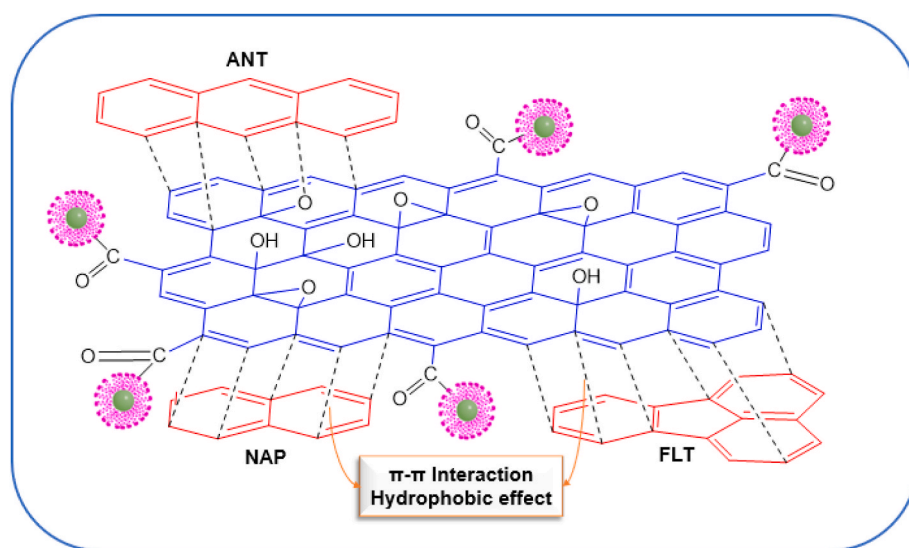
Fig. 10. Adsorption mechanisms of PAHs into G-mCS/GO.

increasing their adsorption capacity into the adsorbents (Wang et al., 2014). The adsorption mechanism of PAHs can also be influenced by the effect of pH and zero charge point; thus, the zeta potentials (ZP) for C-mCS/GO and G-mCS/GO in the presence of naphthalene, anthracene and fluoranthene are shown in Fig. 6d-f. Comparing these results with the ZP before (Fig. 6c) and after adsorption (Fig. 6d-f), it is observed that at pH 4, 6 and 8, there was a decrease in the surface charge of the composites after PAH adsorption, as they have very little negative charge. At pH 10, however, the difference between the ZP values before and after adsorption was very small, which indicates that these suspensions are more negatively charged, which makes them more stable, in accordance with the results presented in the literature (Zhang et al., 2013; Li et al., 2015). In solutions with pH ≥ 10, it is possible that the decrease in the adsorption capacity is associated with the electrostatic repulsion of negative ions, which can reduce the formation of π-π interactions, thus generating a decrease in the adsorptive performance at basic pH (Tang et al., 2021).

4. Challenges, limitations and future prospects

The results and discussions addressed in this study have as the main objective to fill gaps in the literature regarding the development of eco-friendly and low-cost materials based on the principles of green chemistry, aiming at their application for the adsorption of contaminants from wastewater. The results obtained indicated that G-mCS/GO is a potential green adsorbent for the removal of PAHs, presenting competitive adsorption capacities when compared to those of conventional adsorbents. However, it is important to highlight some challenges and limitations that still need to be overcome by green synthesis processes with regard to the application of different natural agents, such as stabilizing, crosslinking or capping agents. In this context, some perspectives for future studies can be proposed to overcome these limitations, such as (i) studies aimed at optimizing the synthesis processes of new green adsorbents, aiming at the application of different natural agents replacing toxic chemical reagents; (ii) application of green materials in dynamic fixed-bed systems, aiming at industrial scale application and treatment of real effluents; and (iii) studies involving the regeneration of these materials in different adsorption cycles.

5. Conclusions

In this study, the synthesis of adsorbents by conventional and green routes (C-mCS/GO and G-mCS/GO, respectively) was performed and then applied to PAH adsorption to investigate their efficiency in naphthalene, anthracene and fluoranthene removal from wastewater. The characterization analyses confirmed the obtainment of magnetic composites with high adsorptive capacities. The results indicate that the application of PAS as a crosslinking agent in the synthesis of G-mCS/GO contributed to improving its thermal and magnetic properties when compared to C-mCS/GO. The adsorption assays showed a better adsorptive capacity of PAHs on G-mCS/GO, for a contact time of 30 min and dosage of adsorbent of 0.1 mg mL^{-1}, mainly for naphthalene and anthracene when compared to the conventional one, with 93.55% and 89.25% removal efficiency, respectively. The affinity assays along with the results of the molecular simulations indicated that the adsorption processes are possibly governed by π-π interactions and hydrophobic effects. In addition, the zeta potential analyses indicated a better adsorption performance at neutral pH. The results obtained in this study point to G-mCS/GO as a novel green composite, which can be applied as an up-and-coming material for the removal of PAHs from wastewater when compared to conventional adsorbents.

CRediT authorship contribution statement

Ruth Nóbrega Queiroz: Methodology, Validation, Methodology, Investigation, Formal analysis, Data curation, Writing - original sketch, Writing – original draft, Writing – review & editing. **Tauany de Figueiredo Neves:** Investigation, Methodology. **Meuris Gurgel Carlos da Silva:** Oversight, Funding acquisition. **Valmor Roberto Mastelaro:** Formal analysis, Investigation. **Melissa Gurgel Adeodato Vieira:** Project administration, Resources, Investigation, Data curation, Writing – review & editing, Funding acquisition. **Patrícia Prediger:** Project administration, Formal analysis, Investigation, Resources, Data curation, Writing – review & editing, Funding acquisition.

Declaration of competing interest

The authors declare that they have no known competing financial interests or personal relationships that could have appeared to influence the work reported in this paper.

Appendix A. Supplementary data

Supplementary data to this article can be found online at https://doi.org/10.1016/j.jclepro.2022.132244.

References

Adeola, A., Forbes, P.B.C., 2022. Assessment of reusable graphene wool adsorbent for the simultaneous removal of selected 2–6 ringed polycyclic aromatic hydrocarbons from aqueous solution. Environ. Technol. 43 (8), 1255–1268. https://doi.org/10.1080/09593330.2020.1824024.

Brião, G.V., Jahn, S.L., Foletto, E.L., Dotto, G.L., 2018. Highly efficient and reusable mesoporous zeolite synthetized from a biopolymer for cationic dyes adsorption.

Colloids Surf. A Physicochem. Eng. Asp. 556, 43–50. https://doi.org/10.1016/j.colsurfa.2018.08.019.

Francisco, W., Ferreira, F.V., Ferreira, E.V., Cividanes, L.S., Coutinho, A.R., Thim, G.P., 2015. Functionalization of multi-walled carbon nanotube and mechanical property of epoxy-based nanocomposite. J. Aero. Technol. Manag. 7, 289–293. https://doi.org/10.5028/jatm.v7i3.485.

Ganguly, A., Sharma, S., Papakonstantinou, P., Hamilton, J., 2011. Probing the thermal deoxygenation of graphene oxide using high-resolution in situ X-ray-based spectroscopies. J. Phys. Chem. C 115, 17009–17019. https://doi.org/10.1021/jp203741y.

Gul, K., Sohni, S., Waqar, M., Ahmada, F., Norulaini, N.A.N., Mohd, Omar, A.K., 2016. Functionalization of magnetic chitosan with graphene oxide for removal of cationic and anionic dyes from aqueous solution. Carbohydr. Polym. 152, 520–531. https://doi.org/10.1016/j.carbpol.2016.06.045.

Guo, Y., Sun, X., Liu, Y., Wang, W., Qiu, H., Gao, J., 2012. One pot preparation of reduced graphene oxide (RGO) or Au (Ag) nanoparticle-RGO hybrids using chitosan as a reducing and stabilizing agent and their use in methanol electrooxidation. Carbon 50, 2513–2523. https://doi.org/10.1016/j.carbon.2012.01.074.

Gurunathan, S., Han, J.W., Kim, E., Kwon, D.N., Park, J.K., Kim, J.H., 2014. Enhanced green fluorescent protein-mediated synthesis of biocompatible graphene. J. Nanobiotechnol. 12, 41–57. https://doi.org/10.1186/s12951-014-0041-9.

Han, Q., Wang, Z., Xia, J., Chen, S., Zhang, X., Ding, M., 2012. Facile and tunable fabrication of Fe$_3$O$_4$/graphene oxide nanocomposites and their application in the magnetic solid-phase extraction of polycyclic aromatic hydrocarbons from environmental water samples. Talanta 101, 388–395. https://doi.org/10.1016/j.talanta.2012.09.046.

Haneef, T., Mustafa, M.R.U., Rasool, K., Ho, Y.C., Kutty, S.R.M., 2020. Removal of polycyclic aromatic hydrocarbons in a heterogeneous fenton like oxidation system using nanoscale zero-valent iron as a catalyst. Water 12 (9), 2430. https://doi.org/10.3390/w12092430.

Hsu, H., Kuo, C., Jehng, J., Wei, C., Wen, C., Chen, J., Chen, L., 2019. Application of Graphene Oxide Aerogel to the Adsorption of Polycyclic Aromatic Hydrocarbons Emitted from the Diesel Vehicular Exhaust, vol. 7, p. 103414. https://doi.org/10.1016/j.jece.2019.103414, 6.

Huang, D., Xu, B., Wu, J., Brookes, P.C., Xu, J., 2019. Adsorption and desorption of phenanthrene by magnetic graphene nanomaterials from water: roles of pH, heavy metal ions and natural organic matter. Chem. Eng. J. 368, 390–399. https://doi.org/10.1016/j.cej.2019.02.152.

Hummers, W.S., Offeman, R.E., 1958. Preparation of graphitic oxide. J. Am. Chem. Soc. 80, 1339. https://doi.org/10.1021/ja01539a017.

Jiang, Y., Gong, J.L., Zeng, G.M., Ou, X.M., Chang, Y.N., Deng, C.H., Zhang, J., Liu, H.Y., Huang, S.Y., 2016. Magnetic chitosan–graphene oxide composite for antimicrobial and dye removal applications. Int. J. Biol. Macromol. 82, 702–710. https://doi.org/10.1016/j.ijbiomac.2015.11.0210.

Kalliola, S., Repo, E., Srivastava, V., Heiskanen, J.P., Sirvio, J.A., Liimatainen, H., Mika Sillanpaa, M., 2017. The pH sensitive properties of carboxymethyl chitosan nanoparticles cross-linked with calcium ions. Colloids Surf. B Biointerfaces 153, 229–236. https://doi.org/10.1016/j.colsurfb.2017.02.025.

Li, B., Ou, P., Wei, Y., Zhang, X., Song, J., 2018. Polycyclic aromatic hydrocarbons adsorption onto graphene: a DFT and AIMD study. Materials 11, 726. https://doi.org/10.3390/ma11050726.

Li, X., Li, F., Fang, L., et al., 2015. Effect of microbes on the adsorption of naphthalene by graphene oxide. J. Nanoparticles. https://doi.org/10.1155/2015/816982.

Li, M.F., Liu, Y.G., Zeng, G.M., Liu, S.B., Hu, X.J., Shu, D., Jiang, L.H., Tan, X.F., Cai, X.X., Yan, Z.L., 2017. Tetracycline absorbed onto nitrilotriacetic acid-functionalized magnetic graphene oxide: influencing factors and uptake mechanism. J. Colloid Interface Sci. 485, 269–279. https://doi.org/10.1016/j.jcis.2016.09.037.

Li, S., Luo, J., Hang, X., Zhao, S., Wan, Y., 2019. Removal of polycyclic aromatic hydrocarbons by nanofiltration membranes: rejection and fouling mechanisms. J. Membr. Sci. 582, 264–273. https://doi.org/10.1016/j.memsci.2019.04.008.

Li, Z., Sellaoui, L., Franco, D., Netto, M.S., Georgin, J., Dotto, G.L., Bajahzar, A., Belmabrouk, H., Petriciolet, A.B., Li, Q., 2020. Adsorption of hazardous dyes on functionalized multiwalled carbon nanotubes in single and binary systems: experimental study and physicochemical interpretation of the adsorption mechanism. Chem. Eng. J. 389, 124467. https://doi.org/10.1016/j.cej.2020.124467.

Mackay, D., Shiu, W.Y., Ma, K.C., et al., 1992. Illustrated handbook of physical-chemical properties and environmental fate for organic chemicals: Polynuclear aromatic hydrocarbons, polychlorinated dioxins and dibenzofurans. Lewis Publishers, Chelsea, Michigan, USA.

Maleki, A., Paydar, R., 2015. Graphene oxide–chitosan bionanocomposite: a highly efficient nanocatalyst for the one-pot three-component synthesis of trisubstituted imidazoles under solvent-free conditions. Roy. Soc. Chem. 5, 33177–33184. https://doi.org/10.1039/c5ra03355a.

Maswanganyi, S., Gusain, R., Kumar, N., Kankeu, E.F., Waanders, F.B., Ray, S.S., 2021. Bismuth molybdate nanoplates supported on reduced graphene oxide: an effective nanocomposite for the removal of naphthalene via Adsorption−Photodegradation. ACS Omega 6, 16783–16794. https://doi.org/10.1021/acsomega.1c01296.

Mishra, P.C., Yadav, A., 2012. Polycyclic aromatic hydrocarbons as finite size models of graphene and graphene nanoribbons: enhanced electron density edge effect. Chem. Phys. 402, 56–68. https://doi.org/10.1016/j.chemphys.2012.04.005.

Naghavi, S.S., Gruhn, T., Alijani, V., Fecher, G.H., Felser, C., Medjanik, K., Kutnyakhov, D., Nepijko, S.A., Schönhense, G., Rieger, R., Baumgarten, M., Müllen, K., 2011. Theoretical study of new acceptor and donor molecules based on polycyclic aromatic hydrocarbons. J. Mol. Spectrosc. 265, 95–101. https://doi.org/10.1016/j.jms.2010.12.004.

Neves, T.F., Dalarme, N.B., Silva, P.M.M., Landers, R., Piconec, C.S.F., Prediger, P., 2020. Novel magnetic chitosan/quaternary ammonium salt graphene oxide composite applied to dye removal. J. Environ. Chem. Eng. 8, 103820. https://doi.org/10.1016/j.jece.2020.103820.

Pal, P., Pal, A., Nakashima, K., Yadav, B.K., 2020. Applications of chitosan in environmental remediation: a review. Chemosphere 266, 128934. https://doi.org/10.1016/j.chemosphere.2020.128934.

Parr, R.G., Pearson, R.G., 1983. Absolute hardness: companion parameter to absolute electronegativity. J. Am. Chem. Soc. 105, 7512–7516. https://doi.org/10.1021/ja00364a005.

Parr, R.G., Szentpály, L.V., Liu, S., 1999. Electrophilicity index. J. Am. Chem. Soc. 121, 1922–1924. https://doi.org/10.1021/ja983494x.

Pearson, R.G., 1992. Chemical hardness and the electronic chemical potential. Inorg. Chim. Acta. 198–200, 781–786. https://doi.org/10.1016/S0020-1693(00)92423-X.

Prediger, P., Cheminski, T., Neves, T.F., Nunes, W.B., Sabino, L., Picone, C.S.F., Oliveira, R.L., Correia, C.R.D., 2018. Graphene oxide nanomaterials for the removal of nonionic surfactant from water. J. Environ. Chem. Eng. 6, 1536–1545. https://doi.org/10.1016/j.jece.2018.01.072.

Queiroz, R.N., Prediger, P., Vieira, M.G.A., 2022. Adsorption of polycyclic aromatic hydrocarbons from wastewater using graphene-based nanomaterials synthesized by conventional chemistry and green synthesis: a critical review. J. Hazard Mater. 422, 126904. https://doi.org/10.1016/j.jhazmat.2021.126904.

Salter, C., Foresman, J.B., 1998. Naphthalene and azulene I: semimicro bomb calorimetry and quantum mechanical calculations. J. Chem. Educ. 75, 1341–1345. https://doi.org/10.1021/ed075p1341.

Santos, C.B.R., Lobato, C.C., Sousa, M.A.C., Macêdo, W.J.C., Carvalho, J.C.T., 2014. Molecular modeling: origin, fundamental concepts and applications using structure-activity relationship and quantitative structure-activity relationship. Rev. Theor. Sci. 2, 91–115. https://doi.org/10.1166/rits.2014.1016.

Santos, N.T.G., Moraes, L.F., Silva, M.G.C., Vieira, M.G.A., 2020. Recovery of gold through adsorption onto sericin and alginate particles chemically crosslinked by proanthocyanidins. J. Clean. Prod. 253, 119925. https://doi.org/10.1016/j.jclepro.2019.119925.

Silva, V.A.J., Andrade, P.L., Silva, M.P.C., Dominguez, A.B., Valladares, L.D.L.S., Aguiar, J.A., 2013. Synthesis and characterization of Fe$_3$O$_4$ nanoparticles coated with fucan polysaccharides. J. Magn. Magn Mater. 343, 138–143. https://doi.org/10.1016/j.jmmm.2013.04.062.

Shahraki, S., Delarami, H.S., Khosravi, F., Nejat, R., 2020. Improving the adsorption potential of chitosan for heavy metal ions using aromatic ring-rich derivatives. J. Colloid Interface Sci. 576, 79–89. https://doi.org/10.1016/j.jcis.2020.05.006.

Sheshmani, S., Ashori, A., Hasanzadeh, S., 2014. Removal of Acid Orange 7 from aqueous solution using magneticgraphene/chitosan: a promising nanoadsorbent. Int. J. Biol. Macromol. 68, 218–224. https://doi.org/10.1016/j.ijbiomac.2014.04.0570.

Shi, Y., Xing, Y., Deng, S., Zhao, B., Fu, Y., Liu, Z., 2020. Synthesis of proanthocyanidins-functionalized Fe$_3$O$_4$ magnetic nanoparticles with high solubility for removal of heavy-metal ions. Chem. Phys. Lett. 753, 137600. https://doi.org/10.1016/j.cplett.2020.137600.

Solano, R.A., León, L.D.D., Ávila, G.D., Herrera, A.P., 2021. Polycyclic aromatic hydrocarbons (PAHs) adsorption from aqueous solution using chitosan beads modified with thiourea, TiO$_2$ and Fe$_3$O$_4$ nanoparticles. Environ. Technol. Innovat. 21, 101378. https://doi.org/10.1016/j.eti.2021.101378.

Song, L., Niu, X., Zhang, N., Li, T., 2021. Effect of biochar-immobilized *Sphingomonas* sp. PJ2 on bioremediation of PAHs and bacterial community composition in saline soil. Chemosphere 279, 130427. https://doi.org/10.1016/j.chemosphere.2021.130427.

Song, T., Weijun Tian, W., Qiao, K., Zhao, J., Chu, M., Du, Z., Wang, L., Xie, W., 2021. Adsorption behaviors of polycyclic aromatic hydrocarbons and oxygen derivatives in wastewater on N-doped reduced graphene oxide. Separ. Purif. Technol. 254, 117565. https://doi.org/10.1016/j.seppur.2020.117565.

Stankovich, S., Dikin, D.A., Piner, R.D., Kohlhaas, K.A., Kleinhammes, A., Jia, Y., Wu, Y., Nguyen, S.T., Ruoff, R.S., 2007. Synthesis of graphene-based nanosheets via chemical reductionof exfoliated graphite oxide. Carbon 45, 1558–1565. https://doi.org/10.1016/j.carbon.2007.02.034.

Subedi, N., Lähde, A., Danso, E.A., Iqbal, J., Bhatnagar, A., 2019. A comparative study of magnetic chitosan (Chi@Fe3O4)andgrapheneoxide modified magnetic chitosan (Chi@Fe3O4GO) nanocomposites forefficient removal of Cr(VI) from water. Int. J. Biol. Macromol. 137, 948–959. https://doi.org/10.1016/j.ijbiomac.2019.06.151.

Tang, T., Cao, S., Xi, C., Chen, Z., 2021. Multifunctional magnetic chitosan-graphene oxide-ionic liquid ternary nanohybrid: an efficient adsorbent of alkaloids. Carbohydr. Polym. 255, 117338. https://doi.org/10.1016/j.carbpol.2020.117338.

Travlou, N.A., Kyzas, G.Z., Lazaridis, N.K., Deliyanni, E.A., 2013. Functionalization of graphite oxide with magnetic chitosan for the preparation of a nanocomposite dye adsorbent. Langmuir 29, 1657–1668. https://doi.org/10.1021/la304696y, 2013.

Umadevi, D., Sastry, G.N., 2011. Molecular and ionic interaction with graphene nanoflakes: a computational investigation of CO$_2$, H$_2$O, Li, Mg, Li$^+$, and Mg^{2+} interaction with polycyclic aromatic hydrocarbons. J. Phys. Chem. C 115, 9656–9667. https://doi.org/10.1021/jp201578p.

Wang, D., Liu, L., Jiang, X., Yu, J., Chen, X., Chen, X., 2015. Adsorbent for p-phenylenediamine adsorption and removal based on graphene oxide functionalized with magnetic cyclodextrin. Appl. Surf. Sci. 329, 197–205. https://doi.org/10.1016/j.apsusc.2014.12.161.

Wang, J., Chen, Z., Chen, B., et al., 2014. Adsorption of polycyclic aromatic hydrocarbons by graphene and graphene oxide nanosheets. Environ. Sci. Technol. 48, 4817–4825. https://doi.org/10.1021/es405227u.

Wang, S., Li, E., Li, J., Du, Z., Cheng, F., 2020. Preparation and coagulation-flocculation performance of covalently bound organic hybrid coagulant with excellent stability. Colloids Surf., A 600, 124966. https://doi.org/10.1016/j.colsurfa.2020.124966.

Wang, Y., Li, L., Luo, C., Wang, X., Duan, H., 2016. Removal of Pb^{2+} from water environment using a novel magneticchitosan/graphene oxide imprinted Pb^{2+}. Int. J. Biol. Macromol. 86, 505–511. https://doi.org/10.1016/j.ijbiomac.2016.01.035.

Yang, F., Liu, Y., Gao, L., Sun, J., 2010. pH-Sensitive highly dispersed reduced graphene oxide solution using lysozyme via an in situ reduction method. J. Phys. Chem. 114, 22085–22091. https://doi.org/10.1021/jp1079636.

Zhang, C., Wu, L., Cai, D., Zhang, C., Wang, N., Zhang, J., Wu, Z., et al., 2013. Adsorption of polycyclic aromatic hydrocarbons (Fluoranthene and Anthracenemethanol) by functional graphene oxide and removal by pH and temperature-sensitive coagulation. Appl. Mater. Interfaces 5 (11), 4783–4790. https://doi.org/10.1021/am4002666.

Zhang, H.P., Yang, B., Wang, Z.M., Xie, C., Tang, P., Bian, L., Dong, F., Tang, Y., 2019. Porous graphene oxide/chitosan nanocomposites based on interfacialchemical interactions. Eur. Polym. J. 119, 114–119. https://doi.org/10.1016/j.eurpolymj.2019.07.032.

Zhang, Q., Zhang, Y., Li, Y., Ding, P., Xu, S., Cao, J., 2021. Green synthesis of magnetite nanoparticle and its regulatory effect on fermentative hydrogen production from lignocellulosic hydrolysate by Klebsiella sp. Int. J. Hydrogen Energy 46, 20413–20424. https://doi.org/10.1016/j.ijhydene.2021.03.142.

Zuo, P.P., Feng, H.F., Xu, Z.Z., Zhang, L.F., Zhang, Y.L., Xia, W., Zhang, W.Q., 2013. Fabrication of biocompatible and mechanically reinforced graphene oxide-chitosan nanocomposite films. Chem. Cent. J. 7, 39. https://doi.org/10.1186/1752-153X-7-39.